Check for updates

Two-dimensional wide-bandgap GeSe₂ vertical ultraviolet photodetectors with high responsivity and ultrafast response speed†

Yong Yan, [ID] * Jie Li, Shasha Li, Mengna Wang, Gaoli Luo, Xiaohui Song, Suicai Zhang, Yurong Jiang, [ID] Ruiping Qin [ID] and Congxin Xia [ID] *

Germanium selenide (GeSe₂), as a typical member of 2D wide bandgap semiconductors (WBSs), shows great potential in ultraviolet (UV) optoelectronics due to its excellent flexibility, superior environmental stability, competitive UV absorption coefficient, and significant spectral selectivity. However, the GeSe₂-based UV photodetector suffers from high operation voltages and low photocurrent, which prevents its practical imaging applications. In this work, we report an elevated photocurrent generation in a vertical stacking graphene/GeSe₂/graphene heterostructure with low operation voltage and low power consumption. Efficient collection of photoexcited carriers in GeSe₂ through graphene electrodes results in outstanding UV detection properties, including a pronounced responsivity of 37.1 A W⁻¹, a specific detectivity of 8.83×10^{11} Jones, and an ultrahigh on/off ratio ($\sim 10^5$) at 355 nm. In addition, building a Schottky barrier between GeSe₂ and graphene and reducing the channel length can increase the photoresponse speed to $\sim$300 μs. These accomplishments set the stage for future optoelectronic applications of vertical 2D WBS heterostructure UV photodetectors.

Introduction

Advanced ultraviolet (UV) photodetectors that convert UV radiation signals into electronic signals are of great significance because they have extensive applications in the fields of military warning, spatial communication, ozone hole monitoring, and so on.[1] In the past decades, wide-bandgap semiconductors (WBGSs), such as ZnO, TiO₂, Ga₂O₃, and SnO₂, have been used as excellent building blocks for UV optoelectronic devices with good responsivity, high specific detectivity, and low noise characteristics.[2–6] However, the oxygen-related hole-trapping state induces a low response speed and poor anti-disturb ability, owing to the large density of defects and dangling bonds at the surface.[7] Recently, 2D wide-bandgap semiconductors (2D WBGSs) have attracted significant attention because of their dangling-bond-free surfaces.[8] For example, Ga₂In₄S₉,[9] NiPS₃,[10] GaPS₄,[11] and BiOBr[12] are potential candidate materials for UV photodetectors. However, the synthesis is usually difficult and expensive owing to the complex chemical composition and structural polymorphism of these materials. It is known that elemental or binary compounds can be a more efficient choice for the preparation of detectors. For instance, hexagonal boron nitride (h-BN) with a direct wide bandgap of

5.9 eV, large absorption coefficient (7.5×10^5 cm⁻¹), superior chemical inertness, shows a promising role in UV photodetection.[12,13]

2D WBGS germanium diselenide, GeSe₂, attracts considerable attention due to its excellent anisotropic properties, high stability, strong nonlinearity, and fast response.[14] Moreover, single layer GeSe₂ has [GeSe₄] tetrahedrons as the basic building blocks. The tetrahedrons form [GeSe₄]ₙ chains by corner-sharing along the *a*-axis, which are connected by [Ge₂Se₈] double tetrahedra by edge-sharing along the *b*-axis, forming an in-plane anisotropic geometry.[15] Zhou *et al.* experimentally verified strong in-plane anisotropic properties of the rhombic GeSe₂ layer.[14] Additionally, Yang *et al.* demonstrated the weak interlayer interaction in GeSe₂.[16] It is well known that the electronic and optical properties of 2D materials are dependent on the layer number from multilayer to monolayer. Recently, exfoliated monolayer GeSe₂ nanosheets have been found to have a direct bandgap of 2.96 eV.[17] Meanwhile, GeSe₂ is a well-defined p-type semiconductor with a hole mobility of 690 cm² V⁻¹ s⁻¹, which is higher than that of most 2D semiconductors.[18] However, the GeSe₂ photodetector shows an ultralow photocurrent ($\sim$pA) potentially retarding its practical application in UV detection, which is still required to be comprehensively improved.

In this study, we constructed a vertical GeSe₂-based heterostructure with graphene (labeled as Gr) electrodes for high-performance UV photodetection. We systematically discussed the carrier transport mechanism in Gr/GeSe₂/Gr devices,

School of Physics, Henan Normal University, Xinxiang, Henan province, China. E-mail: yanyong@htu.edu.cn; xiacongxin@htu.edu.cn

† Electronic supplementary information (ESI) available. See https://doi.org/10.1039/d2na00565d

including direct tunneling (DT) to thermionic emission (TE) transport. The redistribution of space charge is increased by the external electric field, which improves the carrier collection efficiency. Moreover, the graphene electrode enhances the carrier extraction, resulting in an excellent photoresponse with a high responsivity of 7.6×10^3 mA W^{-1}, a detectivity of 5.0×10^{10} Jones, a large on/off ratio ($\sim 10^5$), and a fast response speed of ≈ 0.3 ms under 405 nm laser irradiation. These results provide a scientific approach that directs a valuable way to prepare high-performance UV photodetectors.

Experimental details

Transfer method and device fabrication

Bulk GeSe$_2$ crystals were synthesized by a chemical vapor transport method.[17] The 2D GeSe$_2$ flakes were achieved by mechanical exfoliation from bulk crystals with a poly-dimethylsiloxane (PDMS, Shanghai Onway Technology Co. Ltd) stamp-assisted peeling method.[11] High-quality 90 nm SiO$_2$/p$^+$-Si wafer was used as the substrate. For better material adhesion, the substrate was placed on the micro heater of the transfer platform during the transfer process, and after aligning and placing the graphene in the center of the substrate and the temperature was ramped up to 80 °C, the PDMS stamp was allowed to adhere to the SiO$_2$ surface. The temperature was then cooled down to 40 °C to release the glass slide and PDMS stamp from the SiO$_2$/p$^+$-Si substrate, leaving only the graphene flakes on top of the substrate. Following the same transfer procedure, the exfoliated GeSe$_2$, and graphene were stacked layer by layer forming a Gr/GeSe$_2$/Gr vertical vdW heterostructure. Finally, the devices were annealed at 150 °C for 3 h in a vacuum chamber. Standard photolithography was employed to define the source and drain electrode patterns on the wafer, and a 40 nm Au film was evaporated as the contact metal.

Characterization and measurements

The thickness of 2D nanosheets was identified by optical microscopy and atomic force microscopy (AFM, Dimension Icon, Bruker) in a tapping mode. The Raman spectrum was measured by confocal Raman microscopy (Horiba, Evolution HR, 532 nm laser excitation at room temperature). The elemental analysis was proceeded using SEM (SUPRA40, Carl Zeiss AG) combined with energy-dispersive spectrometry (EDS). The electronic and photoelectronic measurements were performed on a probe station (450PM, Micromanipulator) equipped with a semiconductor characterization system (B1500A, Keysight).

Results and discussion

Fig. 1a shows the schematic diagram of the Gr/GeSe$_2$/Gr FET device, in which a GeSe$_2$ layer is sandwiched between two cross-stacked metallic Gr layers on a 90 nm SiO$_2$/p$^+$-Si wafer. The 2D layers were mechanically exfoliated from GeSe$_2$ and graphite crystals using the polydimethylsiloxane (PDMS) tape. The top and bottom graphene layers serve as the source and drain

electrodes, respectively. The device was encapsulated with hexagonal boron nitride (hBN) layers, avoiding carrier scattering caused by adsorbents and impurities between the vertical heterostructure and insulating the device from the air.[19] The overlapping area is 16.8×7.2 μm^2 and the thickness (d) of the GeSe$_2$ active layer is 70.3 nm. The Raman spectra in Fig. 1c were taken from points A, B, and C, respectively. Three Raman peaks at 95, 116, and 210 cm^{-1} correspond to the A_g typical vibrational modes of β-GeSe$_2$.[20,21] There is no detectable change in the GeSe$_2$ peak position at different positions, indicating no mutual stress effect at the van der Waals interface. The G (1583 cm^{-1}) and 2D (2748 cm^{-1}) peaks were observed at the bottom Gr (9.8 nm, blue line) and the top Gr (4.3 nm, red line) layers, respectively.[22] In addition, the detected stoichiometric ratio of Ge and Se is about 1 : 2 (Fig. S1†). These results confirmed we prepared a high-quality Gr/GeSe$_2$/Gr device by the dry transfer process.

We first investigated the current–voltage (I–V) characteristics of the GeSe$_2$ device with the drain bias voltage sweeping from 0 to ± 5 V. The thickness of the GeSe$_2$ layer was about 70.3 nm (Fig. S2†). A Schottky contact was formed between semi-metallic Gr and 2D GeSe$_2$ (Fig. 2a), which is similar to the contact between Gr and GaN.[23] There are three ways for the charge to be transported through the Schottky barrier: DT, TE, and FN mechanisms.[19,24–28] When -0.5 V < V_{ds} <1.5 V, the current (at $\sim$pA) satisfies the DT mechanism. The carrier transport schematic is shown in Fig. 2e(i). Electrons cannot move across the barrier and only a few carriers can pass through the DT process, generating a small current. The direct tunneling process can be described by[19,29]

$$I_{DT} \propto V \exp\left(-\frac{4\pi d \sqrt{2m^* f_B}}{h} \right) \qquad (1)$$

$$\ln\left(\frac{I_{DT}}{V^2} \right) \propto \ln\left(\frac{1}{V} \right) - \frac{4\pi d \sqrt{2m^* f_B}}{h} \qquad (2)$$

where d is the tunneling barrier thickness and f_B is the tunneling barrier. Fig. 2a shows the linear $\ln(1/V) - \ln(I/V^2)$ curve, which is in agreement with the DT mechanism. When V_{ds} > 1.5 V or V_{ds} < -0.5 V, in Fig. 2a, the ln I–V curve exhibits a linear shape (Fig. S2†), indicating that charge carriers follow the TE mechanism. The TE mechanism shows the relationship between the current and voltage as shown by[30]

$$I = A^* T^2 \exp\left(\frac{qV}{k_0 T} \right) \exp\left(\frac{-q f_B}{k_0 T} \right) \qquad (3)$$

$$\ln I \propto \frac{q}{n k_0 T} (V - f_B) \qquad (4)$$

where A^* is the effective Richardson's constant ($A^* = 4\pi m^* q k_0^2 / h^3$, m^* is the effective carrier mass), q is the unit electron charge, k_0 is the Boltzmann constant, T is temperature, f_B is the effective barrier height, and V is the bias voltage. n is the ideality factor. The slope is equal to e/nkT and allows one to extract the ideality factor n using

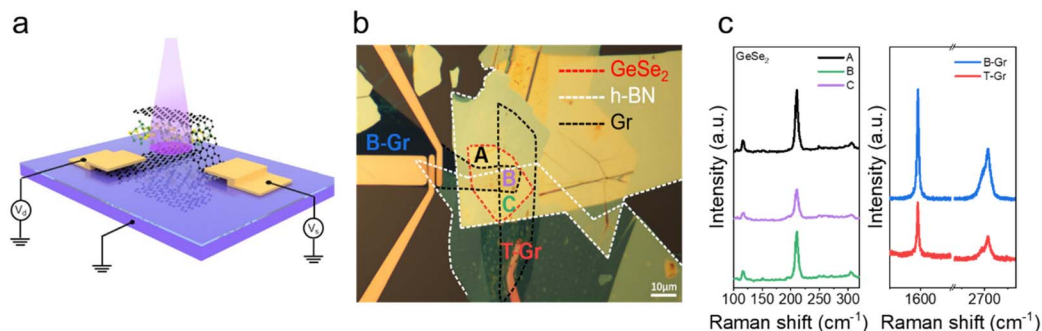$$n = \frac{e}{k_B T} \frac{dV}{d(\ln I)} \qquad (5)$$

Fig. 1 Schematic illustration (a) and optical micrograph (b) of the device with a multilayer GeSe$_2$ semiconductor sandwiched between the T-Gr and B-Gr electrodes. (c) Raman spectra were collected from points A, B, C, bottom Gr, and top Gr, respectively.
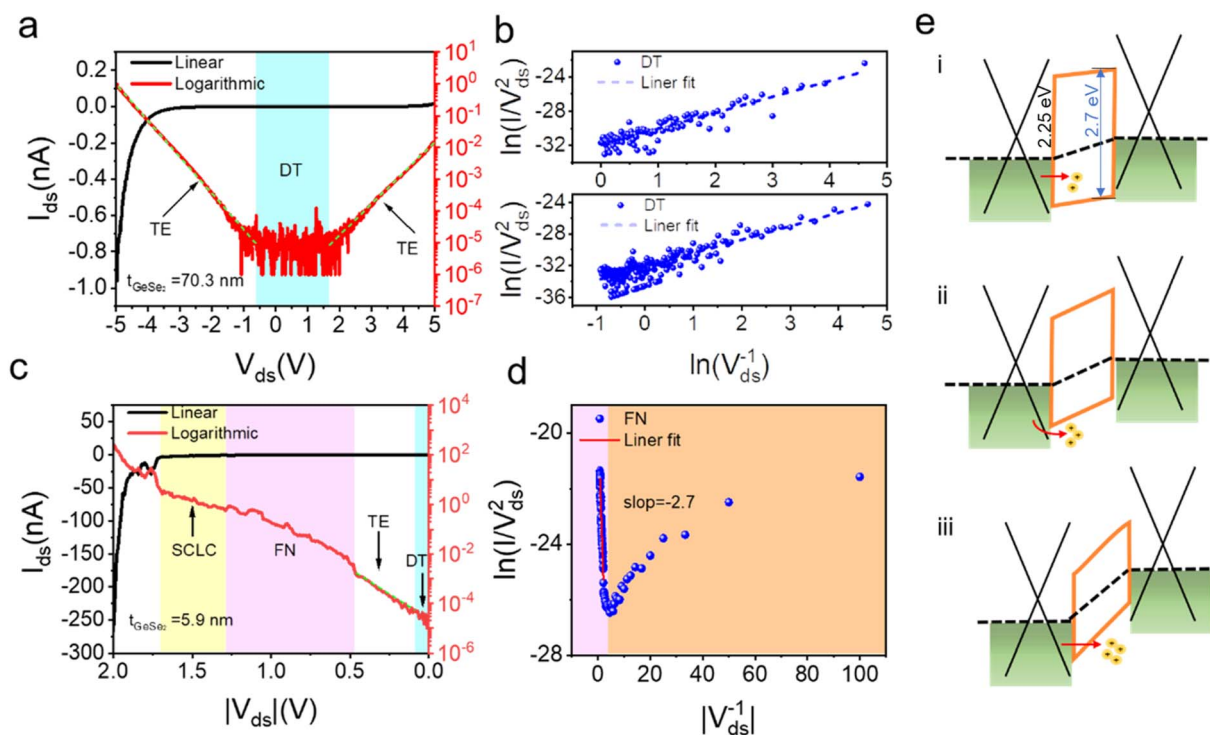

Fig. 2 (a) I–V characteristics of the thick GeSe$_2$ ($d = 70.3$ nm) device, the black and red lines are in linear and logarithmic coordinates, respectively. (b) $\ln(I/V^2)$ vs. $\ln(V_{ds}^{-1})$ plot for the DT behavior. The top panel shows the tunneling current when the drain bias is between -0.5 and 0 V, and the bottom panel shows the tunneling current when the drain bias is between 0 and 1.5 V. (c) I–V characteristics of the GeSe$_2$ ($d = 5.9$ nm) device. (d) $\ln(I/V^2)$ vs. $1/V$ plot (Fowler–Nordheim tunneling plot) when the drain bias is lower than -0.45 V. (e) Schematic illustration of the band diagrams.

Thus, the ideality factor n is 14.3. According to the Shockley–Read–Hall (SRH) recombination theory, the ideality factor of the recombination current is predicted to be $n = 2$ or less, which assumes recombination via isolated point defect levels. The larger ideality factor suggests other recombination currents crossing this Schottky junction.

As the physical properties of 2D materials are sensitive to thickness, we further explored the electrical performance of the device with thin GeSe$_2$ (5.9 nm). When 0 V < V_{ds} < 0.5 V, similar to the thick devices also have DT and TE processes (Fig. S2†). For larger voltage biases (>0.5 V), FN tunneling is expected to

dominate the charge transport. In the FN tunneling mechanism, the tunneling potential is modulated into a triangle barrier and the tunneling current can be described as[19]

$$I_{FN} = \frac{q^3 V^2}{8\pi h f_B} \exp\left(-\frac{8\pi d\sqrt{2m^* f_B^3}}{3qhV}\right) \quad (6)$$

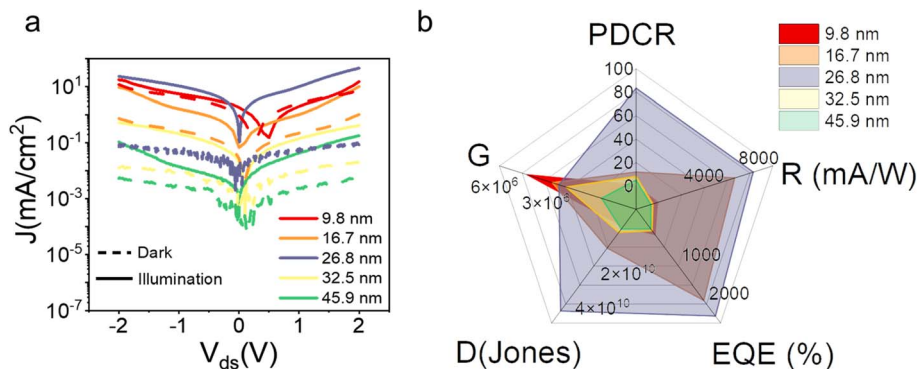$$\ln\frac{I_{FN}}{V^2} = \ln\left(\frac{q^3}{8\pi h f_B}\right) - \frac{8\pi d\sqrt{2m^* f_B^3}}{3qhV} \quad (7)$$

Fig. 3 The optoelectronic performances of the GeSe$_2$ devices with different thicknesses. (a) J–V logarithm plots for the dark state (dashed line) and 405 laser irradiation (solid line). (b) PDCR, responsivity (R), External Quantum Efficiency (EQE), detectivity (D), gain (G) extracted from (a).

In Fig. 2d, the $\ln(I/V^2) - 1/V$ curve is linear with a slope $\frac{8\pi d\sqrt{2m^* f_B^{\,3}}}{3qh} = 2.7$. The effective mass of the hole in the GeSe$_2$ tunneling barrier can be extracted by its band structure fitting as $m^* = 1.8m_0$.[20] The tunneling barrier height f_B can be estimated to be 0.45 eV, confirming the FN tunneling behavior of the hole. The band alignment of Gr/GeSe$_2$ heterostructures shows that the conduction and valence band offsets are 2.25 eV and 0.45 eV, respectively. (Fig. S3†) With the large bias voltage, the energy band renders very strong bending, leading to a shift in transport mechanisms, in which holes can inject into the GeSe$_2$ valence bands.

The optoelectronic properties of the device were then systematically studied to examine its potential application in UV photodetection. Fig. 3a and b present the I–V characterization of the devices based on the GeSe$_2$ thickness-modulation (the corresponding optical images are shown in Fig. S4†). The different current densities are ascribed to the GeSe$_2$ thickness and tunnel junction area. We calculated the current density (J) to normalize the influence of the tunnel area. For the case of the thinnest sample (9.8 nm), the device exhibited a high dark current. As we discussed above, DT is the dominant carrier transport mechanism under small V_{ds}. The tunneling probability (P_{TB}) is evaluated based on the equation[31]

$$P_{TB} = \exp\left(-\frac{2w_{TB}}{\hbar}\sqrt{2m\Phi_{TB}} \right) \tag{8}$$

where $\hbar$ is the reduced Planck's constant, m is the mass of the free carrier, and w_{TB} and Φ_{TB} are the width and height of the potential barrier. There is a bandgap difference of only 0.26 eV between the monolayer and bulk GeSe$_2$.[17] The tunneling probability can be suspected in terms of the barrier width, that is, the thickness. Therefore, the thinner GeSe$_2$ vertical device shows a larger dark current.

Under 405 nm light illumination, all devices exhibit a positive photoresponse because the photon absorption generates electron–hole pairs in GeSe$_2$ layers, which drift in opposite directions towards the graphene electrode. To evaluate the performance of photodetectors, several important parameters are explored quantitatively, including photo-to-dark-current

ratio (PDCR), response (R_λ), external quantum efficiency (EQE), and detectivity (D^*). They are defined as[32–34]

$$\text{PDCR} = \frac{I_{ph} - I_{dark}}{I_{dark}} \tag{9}$$

$$R_\lambda = I_{ph}/P_{in}S \tag{10}$$

$$\text{EQE} = hcR_\lambda/e\lambda \tag{11}$$

$$D^* = R_\lambda S^{\frac{1}{2}} \Big/ (2eI_{dark})^{\frac{1}{2}} \tag{12}$$

$$G = \frac{\tau_{life}}{\tau_{transit}} = \frac{\tau_{life}}{L^2}\mu V_{DS} \tag{13}$$

where I_{ph} is the photocurrent ($I_{illumination} - I_{dark}$), P_{in} is the light power intensity, S is the area of the overlapped region, h is the Planck constant, c is the velocity of light, λ is the wavelength of exciting light, L is the length of the channel (GeSe$_2$ thickness), and μ is the carrier mobility. The 26.8 nm GeSe$_2$ device exhibits a better photoresponse with PDCR = 83.3, R_λ = 7.6A/W, EQE = ~2316%, and D^* = 5.0 × 10^{10} Jones. In general, a thicker sample has a higher absorption coefficient than a thinner one, producing a larger photocurrent. However, it has been reported that an increase in absorption layer thickness will result in a decrease in current gain. The reason is that increasing the thickness uniformly reduces the electric field intensity, resulting in significant reduction in the field-effect drifting of electrons and holes. Consequently, it is still essential to optimize the thickness of GeSe$_2$ layers to function as light absorption and charge separation layers in the future.

To validate the superiority of this Gr/GeSe$_2$/Gr vertical device, one set of comparisons between vertical and planar devices is shown in Fig. 4. The optoelectrical performance of vertical devices is much better than that of the planar device. The short transport channel results in a large electric field, leading to a highly efficient separation for the majority carriers and a high photocurrent. In addition, the vertical device with graphene electrodes shows better performance than that of the device with Au electrodes, which is ascribed to the UV light absorbance of Au electrodes reducing the carrier generation in the GeSe$_2$
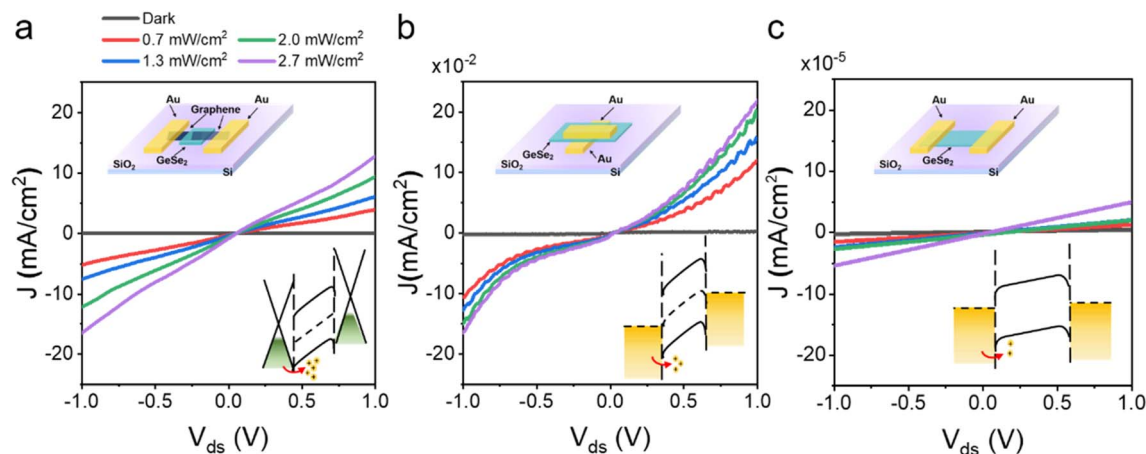
Fig. 4 The electrical performance of three photodetectors with different architectures: (a) Gr/GeSe$_2$/Gr (vertical), (b) Au/GeSe$_2$/Au (vertical), and (c)Au/GeSe$_2$/Au (horizontal), respectively. The inset diagram shows the structure schematic and band diagram.

layer. Therefore, in Gr/GeSe$_2$/Gr devices, the stronger input light and high carrier mobility of Gr layers lead to the devices showing excellent optoelectronic performance which is two orders of magnitude higher than those of the other architectures (see ESI Material Fig. S5† for details).

To demonstrate the spectrum-selective UV photodetection capability of our device, a series of photoelectric measurements were performed at different wavelengths. The time-resolved photoresponse at various wavelengths under the same light power (10 nW) is shown in Fig. 5a. These spectral photocurrent curves indicate an obvious suppression of device responsivity beyond the UV range. Fig. 5b shows the gradual increase in photocurrent with increasing illumination power density. Under an incident light of 2.7 mW cm^{-2}, the I_{light}/I_{dark} ratio has already reached over 1.12×10^5. The photocurrent can be expressed by a power law relationship $I_{ph} \propto P^{0.91}$, as shown in Fig. 5c, suggesting efficient electron–hole pair generation and separation in the GeSe$_2$ layers and Gr/GeSe$_2$ Schottky interface.

The response speed is another pivotal parameter for PDs. We use the rise time (τ_r) and decay time (τ_d) to describe the
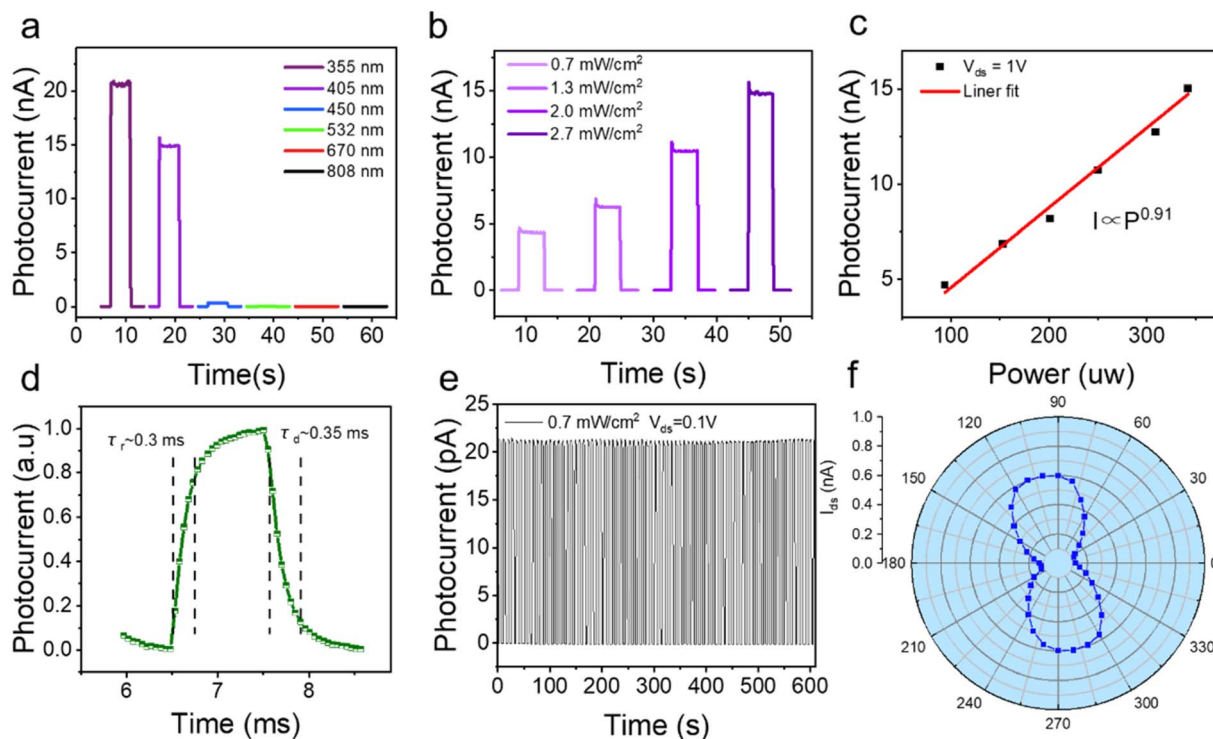

Fig. 5 (a) Photocurrent–time (I–t) response at various wavelengths. (b) I–t response (fixed dc bias: 1 V) under a 405 nm laser with different power intensities. (c) Photocurrent as a function of light power density at V_{ds} = 1 V. (d) A typical photoresponse time curve for the rise time and the fall time. (e) Stability testing. (f) Anisotropic photoresponse under a 405 nm laser.

Table 1 Summary of 2D wide bandgap photodetectors

Materials	Measurement condition	R [mA W^{-1}]	EQE [%]	D^* [Jones]	Response time [ms]	On/off ratio	Ref
GeSe$_2$	355 nm @ 1 V	3.7×10^4	11 300	8.83×10^{11}	0.3/0.35	>10^5	This work
	405 nm @ 1 V	7.6×10^3	2316	5.0×10^{10}			
CdS	400 nm @ 2 V	0.18×10^3	55.87	2.7×10^9	14/8	10^3	35
GaN	325 nm @ 2 V	1367	—	—	152.4/155.3	29.09	36
CaS	254 nm @ 2 V	4.2×10^3	2050	10^{13}	—	—	37
4H–SiC	310 nm @ 5 V	70	33	—	—	—	38
Ga$_2$In$_4$S$_9$	360 nm @ 5 V	111.9×10^3	3.85×10^4	2.25×10^{11}	40/50	2136	9
WS$_2$	365 nm @ 5 V	53.3×10^3	—	1.22×10^{11}	30	2.94×10^4	39
AlN	180 nm @ 5 V	—	—	—	110/80	10^2	32
GQD	254 nm @ 5 V	2.1	—	9.59×10^{11}	64/43	6000	40
ZnS	320 nm @ 5 V	120	50	—	—	—	41
CaTe	375 nm @ 5 V	30	—	—	54	—	42
SnS$_2$	405 nm @ 5 V	0.695	0.22	7.39×10^6	400	—	43
Diamond	210 nm @ 5 V	48	42	—	—	—	44
NiPS$_3$	254 nm @10 V	126	—	1.22×10^{12}	453/384	2×10^2	10
BiOBr	315 nm @ 10 V	12739×10^3	6.46×10^6	8.37×10^{12}	0.102	10^4	12
CuGaS$_2$	254 nm @ 10 V	5.1×10^3	—	1.67×10^{11}	1800/10 100	—	45
Ga$_2$O$_3$	250 nm @ 10 V	37	18	—	—	10^3	6
TiO$_2$	310 nm @ 10 V	3.27	—	—	—	—	4
ZnMgO	260 nm @ 10 V	1.664	—	—	—	—	46
GeSe$_2$	266 nm @ 20 V	200	93	1.6×10^{15}	300	100	17
h-BN	212 nm @ 20 V	0.1	—	2.4×10^8	320/630	10^3	13
CuBr	345 nm @ 30 V	3.17×10^3	1126	1.4×10^{11}	32/48	—	47

response speed. The τ_r and τ_d are defined as the times of current changing between 10% and 90% of the maximum value, respectively. Importantly, the τ_r and τ_d are about 300 μs and 350 μs, which are measured using a home-made system with a voltage of 0.916 V. The system consists of a laser, an optical microscope, a current amplifier, and an oscilloscope. These values are smaller than those of lateral GeSe$_2$ and Ga$_2$O$_3$ PDs. The ultrafast photoresponse of this photodetector is mainly attributed to a strong electric field at the junction between the Gr electrodes and GeSe$_2$ layers, where carriers are spontaneously transferred. The anisotropy of the crystal structure and geometry of GeSe$_2$ nanoflakes will directly lead to the anisotropy of photoelectric transport of carriers. Linearly polarized photodetection was investigated in Fig. 5f under 405 nm polarization illumination. It is clear that by rotating the polarization of the light, the photocurrent changes dramatically. These results further confirm that the photocurrent comes from the GeSe$_2$ layer, which offers us a great opportunity to further exploit GeSe$_2$ in the practical polarization-sensitive photodetector. Table 1 summarizes the performance of the Gr/GeSe$_2$/Gr heterojunction photodetector and some reported photodetectors based on wide bandgap 2D nanomaterials for comparison. Notably, the performances of the Gr/GeSe$_2$/Gr heterojunction photodetector in our work are better than those of the reported wide bandgap 2D nanomaterial-based photodetectors.

Conclusion

In summary, we have fabricated a series of planar and vertical devices based on GeSe$_2$ and Gr layers. Optical microscopy, AFM, Raman spectroscopy, and photoelectric measurements were systematically performed. The carrier transport mechanism of direct tunneling and thermoelectric emission was analyzed in the Gr/GeSe$_2$/Gr device. Compared with the vertical Au/GeSe$_2$/Au, horizontal Au/GeSe$_2$/Au, and other 2D material photodetectors, the vertical Gr/GeSe$_2$/Gr exhibits competitive high performance including an excellent responsivity of 37.1 A W^{-1}, a maximum detectivity of 8.83×10^{11} Jones, a high on/off ratio ($\sim 10^5$) at 355 nm, and a fast response time of $\sim$300 μs. We believe that the GeSe$_2$-based vertical heterostructure will be a good candidate for application in UV photoelectronics.

Conflicts of interest

There are no conflicts to declare.

Acknowledgements

References

1 H. Chen, K. Liu, L. Hu, A. A. Al-Ghamdi and X. Fang, *Mater. Today*, 2015, **18**, 493–502.

2 S. Mitra, Y. Pak, N. Alaal, M. N. Hedhili, D. R. Almalawi, N. Alwadai, K. Loganathan, Y. Kumarasan, N. Lim, G. Y. Jung and I. S. Roqan, *Adv. Opt. Mater.*, 2019, **7**, 1900801.

3 C. Tong, J. Yun, E. Kozarsky and W. A. Anderson, *J. Electron. Mater.*, 2013, **42**, 889–893.

4 H. Huang, Y. Xie, Z. Zhang, F. Zhang, Q. Xu and Z. Wu, *Appl. Surf. Sci.*, 2014, **293**, 248–254.

5 A. Das Mahapatra and D. Basak, *Sens. Actuators, A*, 2020, **312**, 112168.

6 T. Oshima, T. Okuno and S. Fujita, *Jpn. J. Appl. Phys.*, 2007, **46**, 7217–7220.

7 B. Nabet, *Photodetectors: Materials, Devices and Applications in Communications and Imaging Technologies*, Elsevier Science & Technology, 2015.

8 O. Lopez-Sanchez, D. Lembke, M. Kayci, A. Radenovic and A. Kis, *Nat. Nanotechnol.*, 2013, **8**, 497–501.

9 F. Wang, T. Gao, Q. Zhang, Z. Y. Hu, B. Jin, L. Li, X. Zhou, H. Li, G. Van Tendeloo and T. Zhai, *Adv. Mater.*, 2019, **31**, 1806306.

10 J. Chu, F. Wang, L. Yin, L. Lei, C. Yan, F. Wang, Y. Wen, Z. Wang, C. Jiang, L. Feng, J. Xiong, Y. Li and J. He, *Adv. Funct. Mater.*, 2017, **27**, 1701342.

11 Y. Yan, J. Yang, J. Du, X. Zhang, Y. Y. Liu, C. Xia and Z. Wei, *Adv. Mater.*, 2021, **33**, 2008761.

12 C. Gong, J. Chu, S. Qian, C. Yin, X. Hu, H. Wang, Y. Wang, X. Ding, S. Jiang, A. Li, Y. Gong, X. Wang, C. Li, T. Zhai and J. Xiong, *Adv. Mater.*, 2020, **32**, 1908242.

13 H. Liu, J. Meng, X. Zhang, Y. Chen, Z. Yin, D. Wang, Y. Wang, J. You, M. Gao and P. Jin, *Nanoscale*, 2018, **10**, 5559–5565.

14 X. Zhou, X. Hu, S. Zhou, Q. Zhang, H. Li and T. Zhai, *Adv. Funct. Mater.*, 2017, **27**, 1703858.

15 X. W. Zongbao Li, W. Shi, X. Xing, D.-J. Xue and J.-S. Hu, *RSC Adv.*, 2018, **8**, 33445.

16 Y. Yang, X. Wang, S. C. Liu, Z. Li, Z. Sun, C. Hu, D. J. Xue, G. Zhang and J. S. Hu, *Adv. Sci.*, 2019, **6**, 1801810.

17 Y. Yan, W. Xiong, S. Li, K. Zhao, X. Wang, J. Su, X. Song, X. Li, S. Zhang, H. Yang, X. Liu, L. Jiang, T. Zhai, C. Xia, J. Li and Z. Wei, *Adv. Opt. Mater.*, 2019, **7**, 1900622.

18 M. Cao, B. Cheng, Li. Xiao, J. Zhao, X. Su, Y. Xiao and a. S. Leia, *J. Mater. Chem. C*, 2015, **3**, 5207.

19 L. Tong, M. Peng, P. Wu, X. Huang, Z. Li, Z. Peng, R. Lin, Q. Sun, Y. Shen, X. Zhu, P. Wang, J. Xu and L. Ye, *Sci. Bull.*, 2021, **66**, 139–146.

20 Y. Yang, S. C. Liu, W. Yang, Z. Li, Y. Wang, X. Wang, S. Zhang, Y. Zhang, M. Long, G. Zhang, D. J. Xue, J. S. Hu and L. J. Wan, *J. Am. Chem. Soc.*, 2018, **140**, 4150–4156.

21 H. Ouyang, S.-Y. Hu, M.-L. Shen, C.-X. Zhang, X.-A. Cheng and T. Jiang, *Acta Phys. Sin.*, 2020, **69**, 184212.

22 A. C. Ferrari, J. C. Meyer, V. Scardaci, C. Casiraghi, M. Lazzeri, F. Mauri, S. Piscanec, D. Jiang, K. S. Novoselov, S. Roth and A. K. Geim, *Phys. Rev. Lett.*, 2006, **97**, 187401.

23 Z. A. Ansari, T. J. Singh, S. M. Islam, S. Singh, A. K. Pramila Mahala and K. J. Singh, *Optik*, 2019, **182**, 500.

24 J. M. Beebe, B. Kim, J. W. Gadzuk, C. D. Frisbie and J. G. Kushmerick, *Phys. Rev. Lett.*, 2006, **97**, 026801.

25 S.-J. Liang and L. K. Ang, *Phys. Rev. Appl.*, 2015, **3**, 014002.

26 S. Pandey, C. Biswas, T. Ghosh, J. J. Bae, P. Rai, G. H. Kim, K. J. Thomas, Y. H. Lee, P. Nikolaev and S. Arepalli, *Nanoscale*, 2014, **6**, 3410–3417.

27 T. Ikuno, H. Okamoto, Y. Sugiyama, H. Nakano, F. Yamada and I. Kamiya, *Appl. Phys. Lett.*, 2011, **99**, 023107.

28 C. Kim, I. Moon, D. Lee, M. S. Choi, F. Ahmed, S. Nam, Y. Cho, H. J. Shin, S. Park and W. J. Yoo, *ACS Nano*, 2017, **11**, 1588–1596.

29 X. Zhou, X. Hu, S. Zhou, H. Song, Q. Zhang, L. Pi, L. Li, H. Li, J. Lu and T. Zhai, *Adv. Mater.*, 2018, **30**, 1703286.

30 Y. Sun, Z. Jiao, H. J. W. Zandvliet and P. Bampoulis, *J. Phys. Chem. C*, 2022, **126**, 11400–11406.

31 H. Su, T. Hu, F. Wu and E. Kan, *J. Phys. Chem. C*, 2021, **125**, 10738–10746.

32 D. S. Tsai, W. C. Lien, D. H. Lien, K. M. Chen, M. L. Tsai, D. G. Senesky, Y. C. Yu, A. P. Pisano and J. H. He, *Sci. Rep.*, 2013, **3**, 2628.

33 F. Yan, Z. Wei, X. Wei, Q. Lv, W. Zhu and a. K. Wang, *Small Methods*, 2018, **2**, 1700349.

34 M. Buscema, J. O. Island, D. J. Groenendijk, S. I. Blanter, G. A. Steele, H. S. van der Zant and A. Castellanos-Gomez, *Chem. Soc. Rev.*, 2015, **44**, 3691–3718.

35 B. Jin, P. Huang, Q. Zhang, X. Zhou, X. Zhang, L. Li, J. Su, H. Li and T. Zhai, *Adv. Funct. Mater.*, 2018, **28**, 1800181.

36 R. Yu, G. Wang, Y. Shao, Y. Wu, S. Wang, G. Lian, B. Zhang, H. Hu, L. Z. Lei Liu and a. X. Hao, *J. Mater. Chem. C*, 2019, **7**, 14116–14122.

37 P. Hu, L. Wang, M. Yoon, J. Zhang, W. Feng, X. Wang, Z. Wen, J. C. Idrobo, Y. Miyamoto, D. B. Geohegan and K. Xiao, *Nano Lett.*, 2013, **13**, 1649–1654.

38 Y.-Z. Chiou, *Jpn. J. Appl. Phys.*, 2004, **43**, 2432–2434.

39 L. Zeng, L. Tao, C. Tang, B. Zhou, H. Long, Y. Chai, S. P. Lau and Y. H. Tsang, *Sci. Rep.*, 2016, **6**, 20343.

40 Q. Zhang, J. Jie, S. Diao, Z. Shao, Q. Zhang, L. Wang, W. Deng, W. Hu, H. Xia, X. Yuan and a. S.-T. Lee, *IEEE*, 2015, **9**, 1561–1570.

41 X. Fang, Y. Bando, M. Liao, U. K. Gautam, C. Zhi, B. Dierre, B. Liu, T. Zhai, T. Sekiguchi, Y. Koide and D. Golberg, *Adv. Mater.*, 2009, **21**, 2034–2039.

42 Z. Wang, M. Safdar, M. Mirza, K. Xu, Q. Wang, Y. Huang, F. Wang, X. Zhan and J. He, *Nanoscale*, 2015, **7**, 7252–7258.

43 Jia-Jing Wu, Y.-R. Tao, Yi. Wu and X.-C. Wu, *Sens. Actuators, A*, 2016, **231**, 211–217.

44 A. BenMoussa, A. Soltani, K. Haenen, U. Kroth, V. Mortet, H. A. Barkad, D. Bolsee, C. Hermans, M. Richter, J. C. De Jaeger and J. F. Hochedez, *Semicond. Sci. Technol.*, 2008, **23**, 035026.

45 B. Xin, Y. Wu, X. Liu, N. Zhang, H. Yu and W. Feng, *Semicond. Sci. Technol.*, 2019, **34**, 055007.

46 M. M. Fan, K. W. Liu, Z. Z. Zhang, B. H. Li, X. Chen, D. X. Zhao, C. X. Shan and D. Z. Shen, *Appl. Phys. Lett.*, 2014, **105**, 011117.

47 C. Gong, J. Chu, C. Yin, C. Yan, X. Hu, S. Qian, Y. Hu, K. Hu, J. Huang, H. Wang, Y. Wang, P. Wangyang, T. Lei, L. Dai, C. Wu, B. Chen, C. Li, M. Liao, T. Zhai and J. Xiong, *Adv. Mater.*, 2019, **31**, 1903580.